Microporous and Mesoporous Materials 208 (2015) 55–65

Contents lists available at ScienceDirect

Microporous and Mesoporous Materials

journal homepage: www.elsevier.com/locate/micromeso

A combined theoretical and experimental analysis on transient breakthroughs of C_2H_6/C_2H_4 in fixed beds packed with ZIF-7

De-Li Chen [a], Ningwei Wang [a], Chunhui Xu [a], Gaomei Tu [a], Weidong Zhu [a, *], Rajamani Krishna [b, **]

[a] Key Laboratory of the Ministry of Education for Advanced Catalysis Materials, Institute of Physical Chemistry, Zhejiang Normal University, 321004 Jinhua, PR China

[b] Van't Hoff Institute for Molecular Sciences, University of Amsterdam, Science Park 904, 1098 XH Amsterdam, The Netherlands

ARTICLE INFO

Article history:
Received 12 October 2014
Received in revised form
13 January 2015
Accepted 15 January 2015
Available online 29 January 2015

Keywords:
Metal-organic frameworks
ZIF-7
Light alkene and alkane separation
Adsorption-based separation
Breakthrough simulations

ABSTRACT

The selective separation of C_2H_6/C_2H_4 mixtures can be achieved by the zeolitic imidazolate framework ZIF-7, which is a well-known flexible microporous material due to its gate-opening effect in response to external stimuli such as pressure and temperature. Transient breakthrough experiments with C_2H_6/C_2H_4 mixtures were carried out at varying pressure and temperature conditions to confirm the potential application of ZIF-7 to selectively adsorb the saturated alkane and reject the unsaturated alkene in the gas phase during the adsorption cycle. Transient breakthrough simulations, including the influence of intra-crystalline diffusion, were compared with the experimental breakthroughs. The assumption of negligible diffusional limitations is able to capture the essential characteristics of the experimental breakthroughs. With the breakthroughs from both experiments and simulations, the adsorbed amounts of C_2H_6 and C_2H_4 in ZIF-7 were calculated to estimate the separation selectivity, which is in reasonable agreement with ideal adsorbed solution theory calculations. The derived isosteric heats of adsorption for both adsorbates are compared and used to explain the adsorption selectivity for C_2H_6 over C_2H_4 in ZIF-7. The good agreement between experiments and simulations verifies that the simulation methodology employed in the current study is a valuable and efficient tool for modeling the separation performance of C_2H_6/C_2H_4 mixtures in ZIF-7.

1. Introduction

Ethene (C_2H_4) is an important chemical used as feedstock in manufacture of polymers such as polyethene, polyvinyl chloride, polyester, and polystyrene as well as other organic chemicals. Propene (C_3H_6) is also widely used as feedstock in manufacture of polymers such as polypropene. Key processing steps in preparing these feedstocks for polymer productions are the separations of C_2H_6/C_2H_4 and C_3H_8/C_3H_6 mixtures. Due to the small difference in their boiling points between 184.5 K (C_2H_6) and 169.4 K (C_2H_4) as well as 230.9 K (C_3H_8) and 225.4 K (C_3H_6), the separations of C_2H_6/C_2H_4 and C_3H_8/C_3H_6 mixtures via distillation have a low efficiency, in the range of 1.1–1.2. These separations are traditionally carried out by distillation columns that operate at high pressures and low temperatures. The purity requirement of the alkenes as feedstocks to polymerization reactors is 99.95% and consequently the distillation columns are some of the largest and tallest ones used in the petrochemical industry with about 150–200 trays, operating at a reflux ratio of about 15. As a result, the separations of C_2H_4/C_2H_6 and C_3H_6/C_3H_8 mixtures become one of the most energy-intensive processes carried out on a large scale in the chemical industry [1].

Adsorptive separations offer an attractive and energy efficient alternative. Several microporous materials having been studied show potential for the separations of C_2H_4/C_2H_6 and C_3H_6/C_3H_8 mixtures [2–12]. Compared to the alkanes, the corresponding unsaturated alkenes have been found to bind more strongly to metal-organic frameworks (MOFs) with the coordinatively unsaturated metal sites such as Cu-BTC [7,13,14] and M-MOF-74 (M = Mg, Mn, Fe, Co, Ni, Zn) [4,5,15], leading to a high separation selectivity for the alkenes over the alkanes. In addition to the selective adsorption of alkenes using porous adsorbents featuring strong chemical

* Corresponding author. Tel./fax: +86 579 82282932.
** Corresponding author.
E-mail addresses: weidongzhu@zjnu.cn (W. Zhu), r.krishna@contact.uva.nl (R. Krishna).

http://dx.doi.org/10.1016/j.micromeso.2015.01.019
1387-1811/

interactions with C–C double bond in the alkenes, the molecular sieve effect is another important factor to discriminate the alkenes and alkanes, *e.g.* C_3H_6 can be selectively adsorbed over C_3H_8 on the zeolites DD3R [16,17], ITQ-32 [18], and the zeolitic imidazolate framework ZIF-8 [19]. However, a major disadvantage of using these adsorbents is that the desired alkene product, required for the production of polymer grade polyethene and polypropene, can only be recovered in the desorption phase. It becomes necessary to operate with multiple beds involving five different steps; the alkene product with the desired purity is recovered in the final step by counter-current vacuum blowdown [20,21]. The energy requirements for this process are high because of the significantly higher binding energy of the alkenes with the coordinatively unsaturated metal sites than that of the saturated alkanes.

From a practical point of view, it is much more advantageous to have the desired alkene product recovered in the adsorption cycle. Recently published experimental data on the transient breakthroughs of equimolar C_2H_4/C_2H_6 and C_3H_6/C_3H_8 mixtures in adsorber beds packed with ZIF-7 demonstrate that it is possible to recover the pure alkenes in the adsorption cycle [8,9] while for MOFs with the coordinatively unsaturated metal sites the pure alkanes are obtained [4,5,15].

Zeolitic imidazolate frameworks (ZIFs) are very attractive for different separation applications due to their intrinsic properties such as high stability and wide topological variety. Since the successful synthesis of porous ZIFs [22,23], many investigations have been carried out to understand their properties and potential applications on gas sensor [24], catalysis [25], and gas separation [19,26]. ZIFs consist of zeolitic framework topologies, in which all tetrahedral atoms are transition metals (M) interconnected with imidazolate (IM) units, and the M-IM-M angle is very similar to Si–O–Si in many zeolites. Compared to the MOFs with straight tubular channels, ZIFs have advantages in gas separation and storage since they not only have main cavities but also have small apertures separating the larger cavities. It has been reported that ZIF-68, ZIF-69, and ZIF-70, which have a high thermal stability up to 663 K and a high chemical stability, show an unusual selectivity for CO_2 capture from CO_2/CO mixtures [27]. Utilizing the small size (0.34 nm) of the narrow window in ZIF-8, one would expect that gas molecules with kinetic diameters larger than 0.34 nm could be excluded and thus a selective separation is anticipated. However, it has been experimentally observed that molecules with kinetic diameters larger than 0.34 nm, such as CH_4 (0.38 nm) and N_2 (0.36 nm), are adsorbed in this adsorbent, verifying the existence of the structural flexibility of the narrow windows in ZIF-8. More interestingly, Fairen-Jimenez et al. [28] reported that the framework of ZIF-8 could be further changed by the adsorption of N_2 under a high pressure of 1.47 GPa as a result of a swing effect on the imidazolate linkers, which allows more efficient packing of N_2 molecules, leading to an increase of N_2 adsorption by 25.7% [29]. Molecular simulations have been performed to study how the subtle flexibility of ZIF-8 framework affects the adsorption and diffusion of adsorbing molecules, and it has been found that the predicted diffusivities agree well with the experimentally measured data when the flexibility is taken into account [30,31]. This adsorption-induced structural transition of ZIF-8 has been not only identified by experiments [29] but also confirmed by molecular simulations using a flexible force field [32]. Compared to ZIF-8, ZIF-7 has been reported to have an even higher flexibility, known as the gate-opening effect [33–35]. Our previous calculations show that the aperture of ZIF-7 is increased by 0.09 nm with the adsorption of CO_2 at the narrowest site, surrounding by three benzene rings [35]. This high flexibility of the narrow windows in ZIF-7 upon the adsorption of guest molecules is responsible for the step region of adsorption isotherms within a narrow pressure range and the strong adsorption/desorption hysteresis [33,36]. This phenomenon is also applicable to other gases, including N_2O and C_2–C_4 hydrocarbons [9,35].

However, the mechanism of the selective separation of the alkenes over the corresponding alkanes using ZIF-7 has not been completely understood yet, although structural transformations have been observed for ZIF-7 when the guest molecules [H_2O, CO_2, *N*,*N*-dimethylformamide (DMF)] are adsorbed or desorbed [37,38]. Moreover, the theoretical calculations and modeling on the explanation of the experimental observations of the gate-opening effect using ZIF-7 are quite limited [9,35]. The main objective of this study is, therefore, to demonstrate the potential application of ZIF-7 for C_2H_6/C_2H_4 separation using a combined experimental and theoretical method. We first synthesize ZIF-7 and characterize the samples using different techniques. Then, the unary isotherms of C_2H_6 and C_2H_4 at different temperatures are measured and described by a proper isotherm model. The transient breakthroughs at different temperatures and pressures are experimentally determined for C_2H_6/C_2H_4 mixtures through a fixed bed packed with ZIF-7 pellets, and then we focus on simulating the breakthroughs under the same conditions as those for the experiments. The simulated breakthroughs are in good agreement with the experimental ones. Thus the current approach enhances the validity and credibility of the proposed model to describe the separation performance of C_2H_6/C_2H_4 mixtures by ZIF-7.

2. Materials and methods

2.1. Synthesis and characterization of ZIF-7

The synthesis of ZIF-7 was mainly based on the procedure reported by Gücüyener et al. [8], and the detailed synthesis procedure is given elsewhere [35]. Briefly, a solid mixture of $Zn(NO_3)_2 \cdot 6H_2O$ (0.598 g) and benzimidazole (0.479 g) was dissolved in DMF (75 mL) and stirred for a few minutes at room temperature, and then the prepared solution was transferred to a Teflon–lined stainless steel autoclave and the synthesis was carried out without agitation in an oven at 403 K for 48 h. The solid product was then filtered, washed with methanol, and dried at 373 K for one night. The obtained ZIF-7 sample was characterized by powdered X-ray diffraction (XRD) performed on a Phillips PW3040/60 diffractometer using Cu$K\alpha$ radiation ($\lambda = 0.1541$ nm) in a scanning range of 5–50°. The XRD pattern and SEM image of the synthesized ZIF-7 sample are reported elsewhere [35].

2.2. Adsorption isotherm measurement

The unary adsorption/desorption isotherms of C_2H_4 and C_2H_6 on the pellet sample, prepared from the synthesized ZIF-7 sample pressed at 1 MPa and then crushed into particles with sizes from 0.38 to 0.55 mm in diameter, were measured by a Micromeritics ASAP 2020 instrument. About 500 mg of the adsorbent was loaded into the sample cell, and the adsorbent was out gassed under vacuum at 423 K for 10 h prior to the adsorption/desorption measurements. The adsorption/desorption runs were carried out at three different temperatures (273, 298, and 323 K).

2.3. Transient breakthrough experiments

The breakthrough-column setup consists of three sections: a gas mixing and flow control section, a breakthrough column, and an analysis section. The flow–sheet diagram and detailed description of the breakthrough setup are given elsewhere [35,39]. The breakthrough column was installed inside the ceramic oven, which was located inside the convection oven. The external diameter of

the column was 6.35 mm with a length of 15 cm, and the inner diameter was 4.65 mm. A 0.89 g amount of the ZIF-7 pellet sample was packed into the column. The quartz wool was placed at the top and bottom of the column. Prior to the breakthrough experiments, the adsorbent was outgassed overnight at 473 K with a He flow rate of 20 ml (STP) min^{-1} (STP: standard temperature and pressure). The breakthrough curves were then measured by switching the He flow to a flow containing C_2H_6 and C_2H_4 in He (used as a balance) at a total flow rate of 8 ml (STP) min^{-1}. The breakthrough experiments of C_2H_6/C_2H_4 mixtures in He with three different compositions were performed at each temperature while the total pressure of the ternary gas mixtures was maintained at 200 kPa for all the three breakthrough experiments at each temperature. The ratios of C_2H_6/C_2H_4/He were set to 1:1:8 (C_2H_6 and C_2H_4 partial pressures of 20 kPa), 1:1:3 (40 kPa), and 3:3:4 (60 kPa), respectively, at 298 K, while at 323 K, the ratios of C_2H_6/C_2H_4/He were set to 1:1:3 (40 kPa), 3:3:4 (60 kPa), and 4.5:4.5:1 (90 kPa), respectively. These different sets for the breakthrough experiments allow us to understand how the partial pressures of the adsorbing components affect the separation performance. The mass spectrometer (Pfeiffer Vacuum OmniStar GSD 320) in the analysis section was used to monitor the component concentrations continuously. After each breakthrough curve reached the equilibrium, the mixture feed flow of C_2H_6 and C_2H_4 in He was switched back to the He flow with a rate of 20 ml (STP) min^{-1} and the desorption curve was recorded.

The used gases had the following purities: C_2H_6 (99.99%), C_2H_4 (99.99%), and He (99.999%).

2.4. Adsorption selectivity

The measured experimental data on *excess* loadings, q^{excess}, for C_2H_4 and C_2H_6 were first converted into their absolute loadings, q^{abs}, which were then used for fitting with the dual-site Langmuir–Freundlich (DSLF) isotherm model. The fitted adsorption/desorption isotherm data were then used to predict the isosteric heats of adsorption for both C_2H_4 and C_2H_6 as well as the adsorption selectivities using ideal adsorbed sorption theory (IAST). These calculation details and obtained results are presented in the section of Results and discussion.

We develop here the material balance equations for analyzing the transient breakthroughs of C_2H_4/C_2H_6/He mixtures through a column packed with the ZIF-7 pellets. Fig. 1 shows a schematic of the breakthrough column for the experiments. The analysis presented below is essentially that of Pirngruber et al. [40]. From the crystallographic data, the framework or the "grain" density (ρ) of the ZIF-7 pellet is 1241 kg m^{-3}.

Let us consider a column with inner diameter d and length L packed with the ZIF-7 pellets. The cross-sectional area of the column, A, is

$$A = \frac{\pi}{4}d^2 \tag{1}$$

The volume of the empty column, V, is

$$V = AL \tag{2}$$

Let m_{ads} represents the mass of adsorbent ZIF-7 packed into the column. The volume occupied by the adsorbent, V_{ads}, is

$$V_{ads} = \frac{m_{ads}}{\rho} \tag{3}$$

In the breakthrough experiments, the volumetric flow of the inert gas He was maintained constant at a value Q_{He}. The experiments were carried out for a total period of time, t_{ss}, till steady-state was reached. A mass balance for the time interval $t = 0 - t_{ss}$, allows us to determine the component loadings q_i

$$(q_i - q_{i0})m_{ads} = c_t Q_{He}\int_0^{t_{ss}}\left(\frac{y_{i,inlet}}{y_{He,inlet}} - \frac{y_{i,exit}}{\sum_{i=1}^{2}\left(1 - y_{i,exit}\right)}\right)dt - \left(c_t y_{i,exit}\right)(AL - V_{ads}) \tag{4}$$

We assume that the initial loadings of ZIF-7 are q_{i0}. In our "adsorption" experiments $q_{i0} = 0$. The second term on the right hand side represents the "dead volume correction". This correction is properly accounted for in our calculations.

The integral in Eq. (4) can be determined numerically from the breakthrough experimental data. We used numerical quadrature formula, implemented in Excel for the calculations.

The adsorption selectivity can be calculated from

$$S_{ads} = \frac{q_1/q_2}{c_{10}/c_{20}} \tag{5}$$

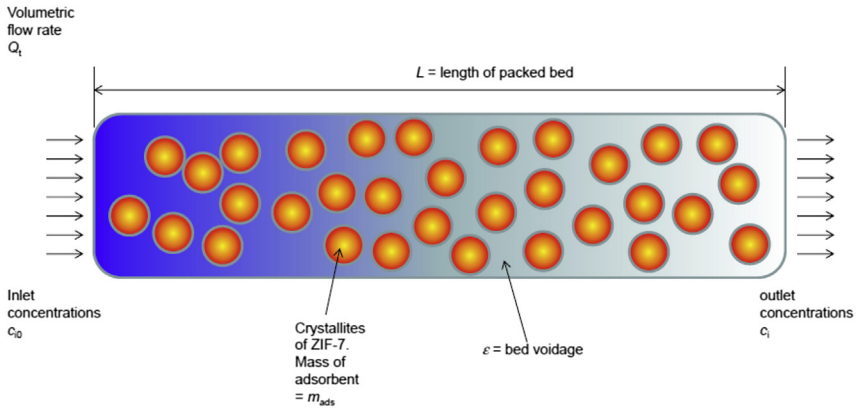

Fig. 1. Schematic of the experimental breakthrough column.

3. Results and discussion

3.1. Adsorption isotherms

The measured experimental data on excess loadings, q^{excess}, of the pure components C_2H_4 and C_2H_6 in ZIF-7, were first converted to absolute loadings, q^{abs}, using

$$q^{abs} = q^{excess} + \frac{pV_{pore}}{ZRT} \quad (6)$$

where Z is the compressibility factor. The Peng-Robinson equation of state was used to estimate Z. The accessible pore volume within the pellets, V_{pore}, was taken to be equal to 0.185 $cm^3\ g^{-1}$, determined from molecular simulations of the crystal structure.

The pure component isotherm data for C_2H_4 and C_2H_6 in ZIF-7, expressed in terms of *absolute* loading, were fitted separately for the *adsorption* and *desorption* branches with the DSLF isotherm model

$$q = q_{A,sat}\frac{b_A p^{\nu_A}}{1 + b_A p^{\nu_A}} + q_{B,sat}\frac{b_B p^{\nu_A}}{1 + b_B p^{\nu_A}} \quad (7)$$

where $q_{A,sat}$, b_A, and ν_A are the saturation capacity, the equilibrium constant, and the exponent in the Langmuir-Freundlich isotherm on the first set of sites (A), respectively, and $q_{B,sat}$, b_B, and ν_B are the analogous parameters on the second set of sites (B). The values of the fitted parameters are reported in Tables 1–3 at 273, 298, and 323 K, respectively. Figs. 2–4 compare the experimental isotherm data at 273, 298, and 323 K with the corresponding DSLF isotherm fits. We note that the fits are excellent over the entire range of pressures at all the three temperatures. The fitted isotherms are used for predicting the isosteric heat of adsorption for each component and IAST selectivities for the mixtures.

The comparison of the adsorption/desorption isotherms between C_2H_6 and C_2H_4 at 273 K is shown in Fig. 2, from which both similarities and differences are observed. The saturation adsorption loadings of C_2H_6 and C_2H_4 are very similar to each other, with values of 2.24 and 2.20 mol kg^{-1} (see Table 1), respectively, estimated on the basis of the DSLF model. The adsorption-desorption isotherms for both C_2H_6 and C_2H_4 form hysteresis loops but with different pressure ranges and widths. The hysteresis loop for C_2H_4 is wider than that for C_2H_6 and it requires a higher pressure (10 kPa) to "open" the gates of ZIF-7 for C_2H_4 than C_2H_6 (about 3 kPa). At 298 K (Fig. 3), the uptakes of C_2H_6 and C_2H_4 at 100 kPa are 1.95 and 1.92 mmol g^{-1}, respectively, very close to the literature data [8]. The threshold pressure associated with the gate-opening induced by C_2H_6 is about 12 kPa, smaller than 30 kPa by C_2H_4, both of which are much higher than those at 273 K. In addition, the shifts of the hysteresis loops to the higher pressures, accompanying with their wider hysteresis loops, are observed as the temperature increases for the adsorption-desorption of both C_2H_6 and C_2H_4 in ZIF-7. Similar to the case at 273 K, the hysteresis loop for C_2H_4 is shifted to a higher pressure at 298 K, compared to that for C_2H_6. When the temperature is further increased to 323 K, as shown in Fig. 4, the hysteresis loops for both C_2H_6 and C_2H_4 are further shifted to higher pressures and the hysteresis loops are even wider, but the threshold pressure (*i.e.*, the gate-opening pressure) of C_2H_4 is still higher than that of C_2H_6. The relatively larger threshold pressure of C_2H_4 could be explained by its smaller adsorption affinity, of which the phenomenon is similar to the reported one for the adsorption of various adsorbates (Xe, CH_4, and CO_2) in MIL-53 with the breathing effects [41]. It was reported that in the temperature–vapor pressure phase diagram for the adsorption of CH_4 and CO_2 in MIL-53, as the temperature goes higher, the pressure range of the narrow pore phase tends to be wider. This explanation well illustrates the phenomenon of the adsorption-desorption isotherms of various adsorbates in MIL-53, which may hold true for elucidating our similar observations for C_2H_6 and C_2H_4 adsorption/desorption in ZIF-7. Compared to C_2H_4, C_2H_6 has a larger adsorption induced stress and thus has a smaller threshold pressure for opening the gates in ZIF-7. A temperature dependent stress model [41] could be a useful tool to explain the origin of wider hysteresis loops at higher temperatures, which is out of the scope in this study. In summary, the different hysteresis loops between C_2H_6 and C_2H_4 imply that the selective separation of C_2H_6 over C_2H_4 using ZIF-7 could be plausible and the different separation efficiencies at different temperatures could be obtained, which will be verified by the breakthrough experiments and simulations.

3.2. Isosteric heat of adsorption

Computation of the adsorption affinity of gas molecules to the nanoporous materials would be helpful to understand the adsorption selectivity. The isosteric heat of adsorption, Q_{st}, defined as

$$Q_{st} = RT^2\left(\frac{\partial \ln p}{\partial T}\right)_q \quad (8)$$

was determined using the pure component isotherm fits. The plots of Q_{st} as a function of loading, determined from both "adsorption" and "desorption" branches of the isotherms for C_2H_6 and C_2H_4, are shown in Fig. 5. The Q_{st} value reflects the adsorption affinity of the adsorbed molecule to ZIF-7. From the data in Fig. 5, we conclude that the adsorption affinity of C_2H_6 is stronger than that of C_2H_4 at the loadings less than 0.2 mol kg^{-1}, under which the gates in ZIF-7 are not "opened" yet, as reflected in Figs. 2–4. In another word, the gas molecules are mostly adsorbed on the surface of the ZIF-7 crystals when the loading is smaller than 0.2 mol kg^{-1}, where C_2H_6 binds stronger to the surface of the ZIF-7 crystals than C_2H_4. Furthermore, as shown in Fig. 5, the Q_{st} of C_2H_6 is larger than that of C_2H_4 as the adsorption loading increases, indicating its stronger adsorption affinity for C_2H_6 in ZIF-7. The density functional theory based calculations suggest that the adsorption energy of C_2H_6 at an energetically favorable site is larger than that of C_2H_4 by about 7 kJ mol^{-1} [9]. The different adsorption energies between these two

Table 1
Estimated values of the parameters in the DSLF isotherm fits for the adsorption and desorption branches of C_2H_4 and C_2H_6 in ZIF-7 at 273 K.

	Site A			Site B		
	$q_{A,sat}$ mol kg^{-1}	b_A $Pa^{-\nu_A}$	ν_A Dimensionless	$q_{B,sat}$ mol kg^{-1}	b_B $Pa^{-\nu_B}$	ν_B dimensionless
C_2H_4, adsorption branch	1.64	1.94×10^{-38}	9.1	0.56	2.3×10^{-5}	1
C_2H_4, desorption branch	1.64	1.62×10^{-36}	9.1	0.56	2.54×10^{-5}	1
C_2H_6, adsorption branch	1.64	3.95×10^{-83}	22.7	0.6	2.98×10^{-5}	1
C_2H_6, desorption branch	1.64	2.41×10^{-79}	22.7	0.6	2.92×10^{-5}	1

Table 2
Estimated values of the parameters in the DSLF isotherm fits for adsorption and desorption branches of C_2H_4 and C_2H_6 in ZIF-7 at 298 K.

	Site A			Site B		
	$q_{A,sat}$ mol kg^{-1}	b_A Pa$^{-\nu_A}$	ν_A Dimensionless	$q_{B,sat}$ mol kg^{-1}	b_B Pa$^{-\nu_B}$	ν_B Dimensionless
C_2H_4, adsorption branch	1.73	6.1×10^{-44}	9.47	0.17	4.09×10^{-5}	1
C_2H_4, desorption branch	1.56	4.6×10^{-40}	9	0.65	1.32×10^{-5}	1
C_2H_6, adsorption branch	1.55	7.15×10^{-65}	15.5	15	3.83×10^{-7}	1
C_2H_6, desorption branch	1.57	1.04×10^{-49}	12.5	0.4	5.0×10^{-8}	1.7

Table 3
Estimated values of the parameters in the DSLF isotherm fits for adsorption and desorption branches of C_2H_4 and C_2H_6 in ZIF-7 at 323 K.

	Site A			Site B		
	$q_{A,sat}$ mol kg^{-1}	b_A Pa$^{-\nu_A}$	ν_A Dimensionless	$q_{B,sat}$ mol kg^{-1}	b_B Pa$^{-\nu_B}$	ν_B Dimensionless
C_2H_4, adsorption branch	1.48	1.31×10^{-74}	14.9	0.88	2.92×10^{-6}	1
C_2H_4, desorption branch	1.37	8.29×10^{-73}	15	3.6	8.38×10^{-7}	1
C_2H_6, adsorption branch	1.5	8.63×10^{-67}	14.5	1	3.5×10^{-6}	1
C_2H_6, desorption branch	1.5	2.06×10^{-72}	16.4	1.1	4.39×10^{-6}	1

adsorbates in ZIF-7 serve to explain the variation of the adsorption selectivities based on IAST predictions to be discussed below.

3.3. Experimental breakthroughs

The breakthrough experiments were carried out to evaluate the separation performance of C_2H_6/C_2H_4 mixtures using fixed beds packed with ZIF-7 pellets. The experiments were conducted using C_2H_6/C_2H_4/He gas mixtures. The total flow rate was held constant at 8 ml (STP) min^{-1} and the total pressure of the ternary gas mixture was maintained at 200 kPa for all three breakthrough experiments at 298 K. The partial pressures of C_2H_6 and C_2H_4 were varied from 20 to 40 and 60 kPa at the inlet of the column by altering the molar ratios of the C_2H_6/C_2H_4/He mixtures from 1:1:8 to 1:1:3 and 3:3:4, respectively. For partial pressures of 20 kPa at 298 K, the mole fraction of C_2H_4 in the outlet of the column is larger than that of C_2H_6 before reaching the steady state, as shown in Fig. 6a, which could be explained as follows: with an inlet C_2H_6 partial pressure of 20 kPa, the gates of ZIF-7 are opened, allowing C_2H_6 molecules to enter the main cavity, while the partial pressure of C_2H_4 keeps increasing until the higher threshold pressure (>30 kPa) of C_2H_4 is reached. Therefore, both mole fractions in the outlet of the column slowly increase until the main cavities are fully filled with C_2H_6 and C_2H_4 but the competing adsorption seems to be favorable for C_2H_6, resulting in a lower concentration of C_2H_6 in the outlet of the column. Finally, the mole fractions of both species increase again, where the main cavities of ZIF-7 are almost saturated. When the partial pressures of both C_2H_6 and C_2H_4 are increased to 40 kPa, which are higher than the gate-opening pressures of both C_2H_6 and C_2H_4, some interesting features are obtained. As shown in Fig. 6a, the measured C_2H_4 mole fraction keeps increasing in the outlet of the column (0–2000 s) while C_2H_6 mole fraction firstly increases and then gradually decreases, indicating more C_2H_6 molecules are adsorbed in the column, which could be explained as the competing adsorption of C_2H_6 over C_2H_4. When the adsorption of C_2H_6 in the column is close to a maximum loading at about 2000 s, the mole fraction of C_2H_6 in the outlet of the column sharply increases until an equilibrium value (0.2) is reached, while a steep roll-up curve is found for C_2H_4 with the largest mole fraction of 0.22 at about 2000 s and then drops sharply to 0.2 at equilibrium. The roll-up phenomenon could be explained as the competitive adsorption of C_2H_6 over C_2H_4, where some of the adsorbed C_2H_4 molecules are replaced with C_2H_6 ones. When the partial pressures of both C_2H_6 and C_2H_4 in the inlet of the column are further increased to 60 kPa, the shapes of the measured breakthrough curves are similar to those at partial pressures of 40 kPa, however, the roll-up phenomenon is pronounced at the higher pressures, as shown in Fig. 6a, indicating the larger partial pressure (over the

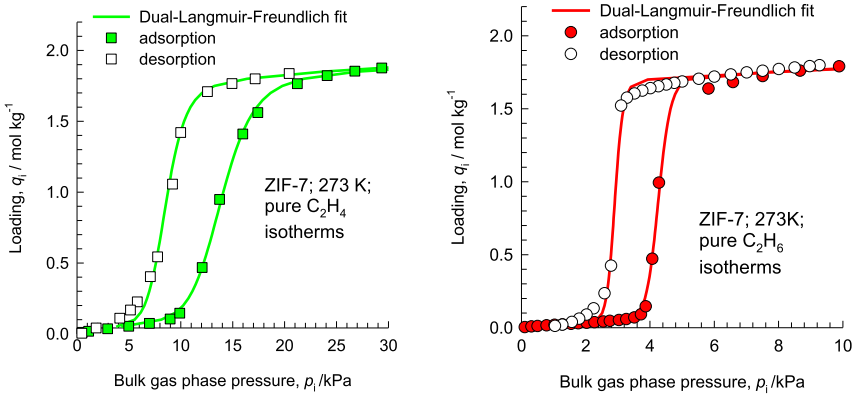

Fig. 2. Comparison of the experimentally determined absolute component loadings of C_2H_4 (left) and C_2H_6 (right) for both adsorption and desorption branches at 273 K with the isotherm fits by the DSLF model using the parameters specified in Table 1.

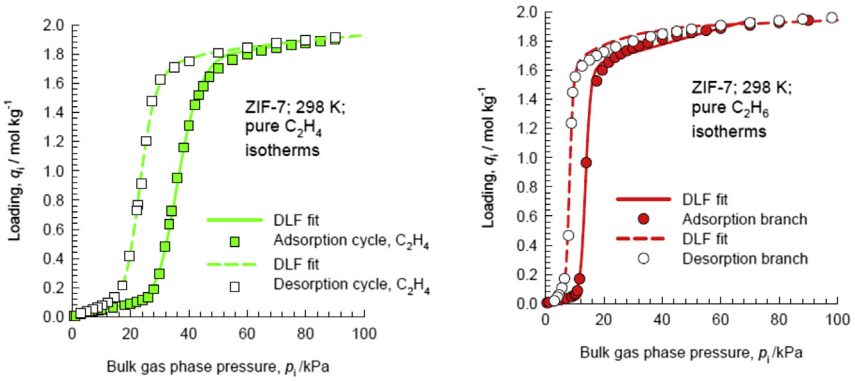

Fig. 3. Comparison of the experimentally determined absolute component loadings of C_2H_4 (left) and C_2H_6 (right) for both adsorption and desorption branches at 298 K with the isotherm fits by the DSLF model using the parameters specified in Table 2.

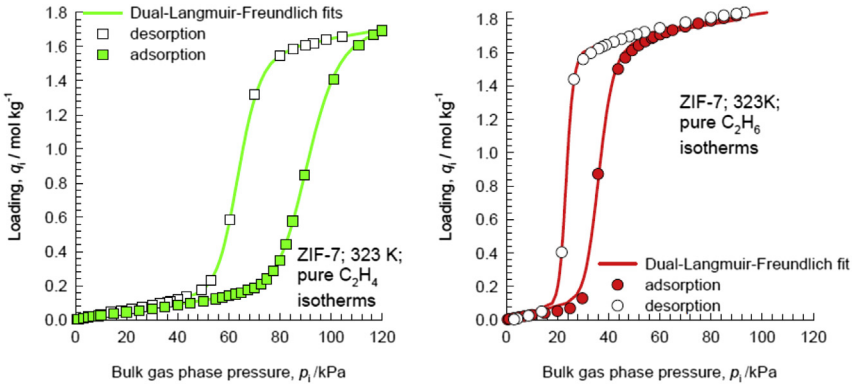

Fig. 4. Comparison of the experimentally determined absolute component loadings of C_2H_4 (left) and C_2H_6 (right) for both adsorption and desorption branches at 298 K with the isotherm fits by the DSLF model using the parameters specified in Table 3.

threshold pressure) facilitates the gas mixture separation, of which the phenomenon is similar to that for N_2O/CO_2 [35].

At 323 K, the behaviors of the breakthrough experiments at three different partial pressures of 40, 60, and 90 kPa, as shown in Fig. 6b, are very similar to those at 298 K, but the separation efficiency under the same partial pressure at 323 K is lower than that at 298 K, which is a result of the higher gate-opening pressure with increasing temperature, as discussed above. This is further confirmed by the computation of the adsorption selectivity based on the calculated adsorption loadings of C_2H_6 and C_2H_4 from the experimental breakthroughs, the so-called experimental selectivity. As shown in Fig. 7a, under the same total hydrocarbon pressures, the C_2H_6/C_2H_4 adsorption selectivity at 298 K is slightly higher than that at 323 K. The results in Fig. 7a show that the experimental selectivities are in the range of 1.5–1.9 at the different temperatures and the three different total hydrocarbon pressures investigated. The IAST adsorption selectivities for 50:50 C_2H_6/C_2H_4 mixture at 298 and 323 K are plotted as a function of total hydrocarbon pressure in Fig. 7b, showing the adsorption selectivity of the C_2H_6/C_2H_4 mixture sharply increases till a total hydrocarbon pressure (p_t) of 25 kPa. As shown in Fig. 3, the gate-opening pressure for C_2H_6 at 298 K is about 12 kPa while for C_2H_4 it is much higher, about 30 kPa. Thus, it is reasonable to expect that C_2H_6 reaches its gate-opening pressure first, and thereafter the adsorption uptake of C_2H_6 should be higher than that of C_2H_4, leading to a sharp increase in adsorption selectivity. As the total hydrocarbon pressure is beyond 30 kPa, C_2H_4 starts adsorbed in ZIF-7, and thus the adsorption selectivity slightly decreases as the total hydrocarbon pressure increases. The trend of the IAST selectivity at 323 K is similar to that at 298 K, with the shift of the largest adsorption selectivity value to a relatively higher pressure. Compared to the experimental selectivity, an IAST selectivity of 2.2–2.4 within the pressure range of 20–200 kPa is only slightly higher, indicating the validation of the IAST calculations in the current case.

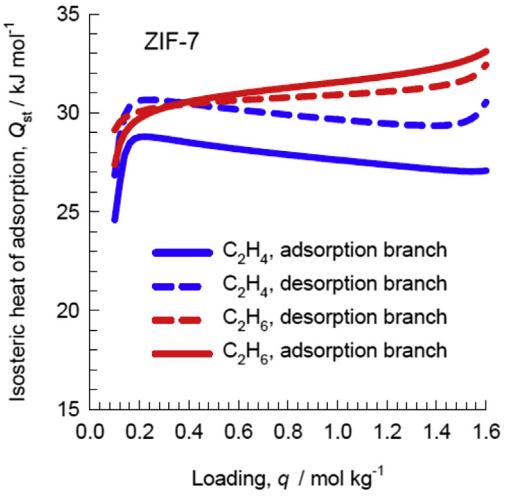

Fig. 5. Isosteric heat of adsorption as a function of loading for C_2H_6 and C_2H_4 in ZIF-7 calculated from the adsorption and desorption isotherms using the Clausius–Clapeyron equation.

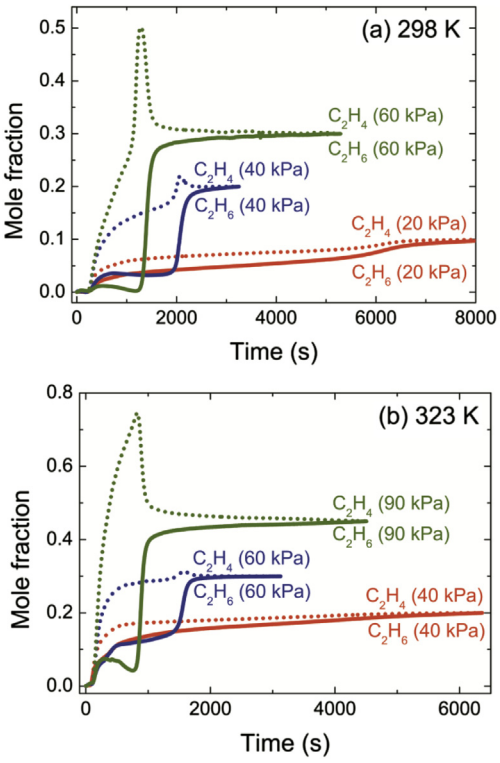

Fig. 6. Adsorption breakthrough profiles for (a) C_2H_6 and C_2H_4 in He with ratios of C_2H_6/C_2H_4/He set to 1:1:8 (C_2H_6 and C_2H_4 partial pressures of 20 kPa), 1:1:3 (40 kPa), and 3:3:4 (60 kPa), respectively, at 298 K, and (b) C_2H_6 and C_2H_4 with ratios of C_2H_6/C_2H_4/He set to 1:1:3 (40 kPa), 3:3:4 (60 kPa), and 4.5:4.5:1 (90 kPa), respectively, at 323 K.

From a practical point of view, it is also very important for the regeneration process to have high efficiency and low energy cost. To understand how ZIF-7 performs on the desorption process of the adsorbed components from the ZIF-7 bed, we carried out the desorption experiments by supplying a stream of pure He to flush the column at a flow rate of 20 ml (STP) min^{-1}, after the adsorption breakthroughs reached the steady state. In all the cases, the desorption curves show that the concentration of the weaker adsorbed C_2H_4 declines faster than that of C_2H_6, and Fig. 8, for example, represents this feature. Interestingly, there are the "roll-up" phenomena available in the C_2H_6 desorption curves, which might be ascribed to the gate-opening effect of ZIF-7.

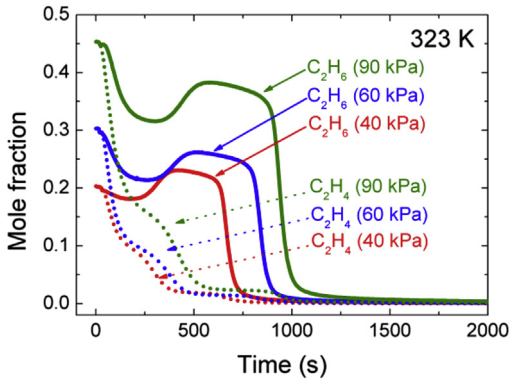

Fig. 8. Measured mole fractions of C_2H_6 and C_2H_4 in the outlet of the column from the three desorption experiments at 323 K as a function of time, where both C_2H_6 and C_2H_4 inlet partial pressures for the breakthrough experiments are 40, 60, and 90 kPa, respectively.

3.4. Comparison of experimental breakthroughs with breakthrough simulations

Figs. 9 and 10 show a comparison between experimental breakthroughs and breakthrough simulations for C_2H_6/C_2H_4/He mixtures at 298 and 323 K, respectively. The details for the breakthrough simulation methodology are given in Supplementary material. The continuous solid lines represent the simulations assuming negligible diffusional limitations and the dashed lines are for the simulations with the inclusion of intra-crystalline diffusion effects. For this purpose, we take $\frac{D_1}{r_c^2} = \frac{D_2}{r_c^2} = 0.0005\ s^{-1}$. The chosen diffusivity values are guided by our previous work [3] that has examined the diffusion effects on the separation performance of $C_2H_6/C_2H_4/H_2$ mixtures in ZIF-7, based on the experimental breakthrough data of Gücüyener et al. [8].

The introduction of diffusional limitations leads to slightly more distended breakthrough characteristics. In all cases, the assumption of negligible diffusional limitations is able to capture the essential characteristics of the experimental breakthroughs. This provides a rationale for Fig. 7b showing that the C_2H_6/C_2H_4 adsorption selectivity in the experiments is only slightly lower than that predicted by IAST.

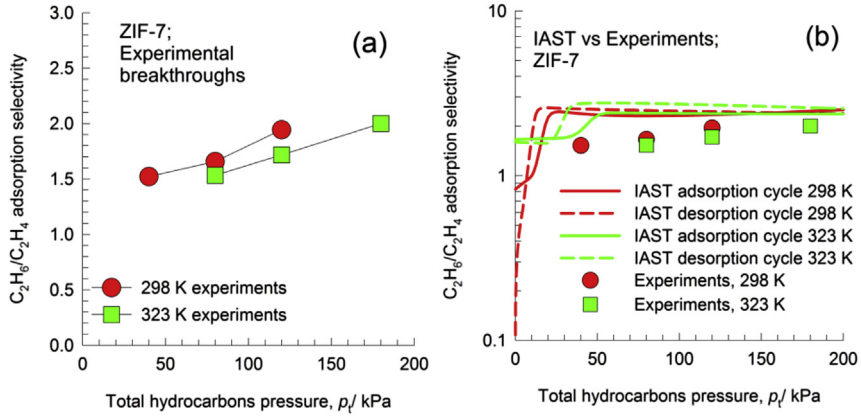

Fig. 7. (a) Comparison of the C_2H_6/C_2H_4 adsorption selectivities determined from the breakthrough experiments at 298 and 323 K and (b) comparison of the C_2H_6/C_2H_4 adsorption selectivities between experiments and IAST predictions.

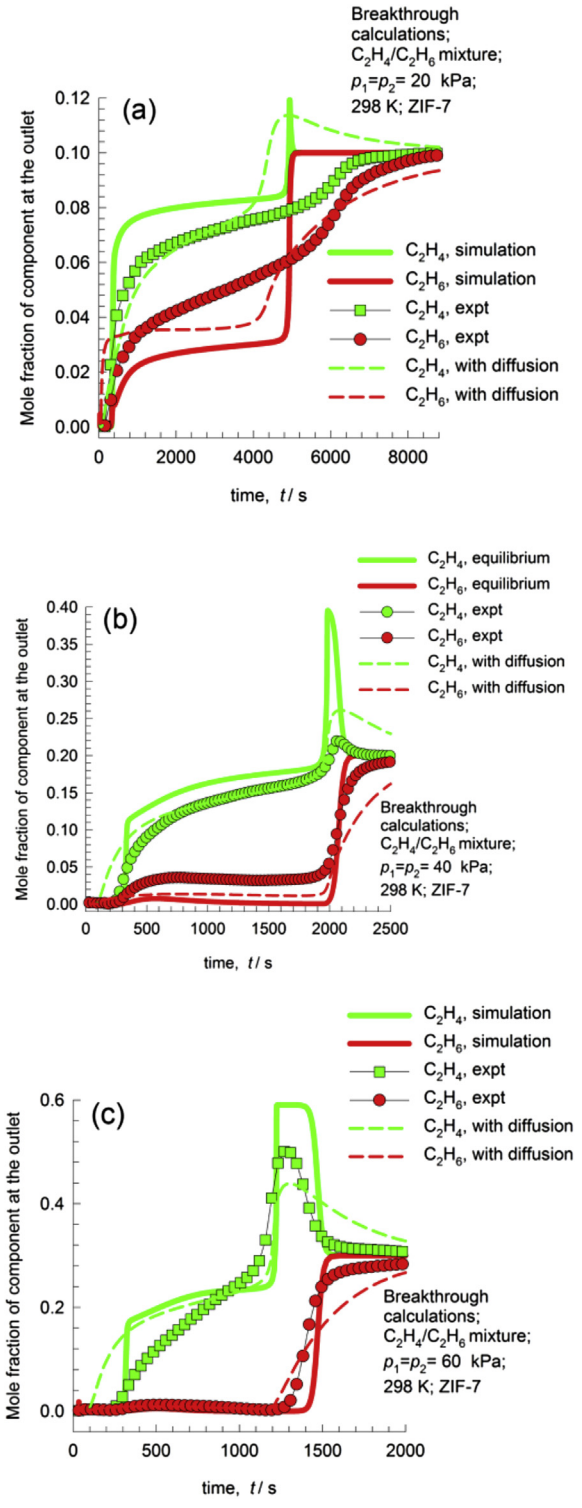

Fig. 9. Comparison of the experimental breakthroughs for C_2H_4/C_2H_6/He with the corresponding breakthrough simulations at 298 K and a total pressure of 200 kPa. (a) p_1 (partial pressure of C_2H_4) = p_2 (partial pressure of C_2H_6) = 20 kPa, and p_3 (partial pressure of He) = 160 kPa; (b) $p_1 = p_2 = 40$ kPa, and $p_3 = 120$ kPa; (c) $p_1 = p_2 = 60$ kPa, and $p_3 = 80$ kPa. The continuous solid lines are the simulations assuming negligible diffusional limitations and the dashed lines are the simulations with the consideration of intra-crystalline diffusion effects. For this purpose we take $\frac{D_1}{r_c^2} = \frac{D_2}{r_c^2} = 0.0005\ s^{-1}$. A video animation of the transient breakthrough at 298 K and $p_1 = p_2 = 60$ kPa, and $p_3 = 80$ kPa is available as Supplementary material.

In Figs. 9 and 10, the isotherm fits used correspond to those for the "adsorption" branch of the component isotherms. In order to gain further insights into the influence of the gate opening on the transient breakthroughs, Figs. 11 and 12 compare the experimental breakthroughs with two scenarios for the simulations: Scenario A

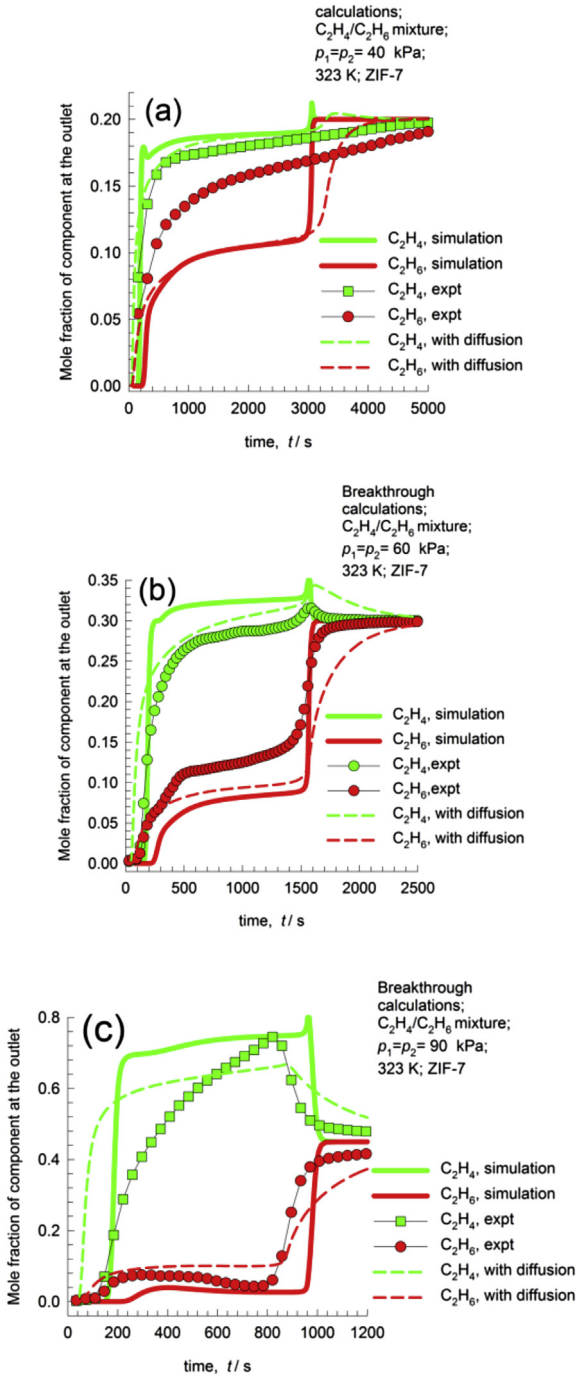

Fig. 10. Comparison of the experimental breakthroughs for C_2H_4/C_2H_6/He with the corresponding breakthrough simulations at 323 K and a total pressure of 200 kPa. (a) p_1 (partial pressure of C_2H_4) = p_2 (partial pressure of C_2H_6) = 40 kPa, p_3 (partial pressure of He) = 120 kPa; (b) $p_1 = p_2 = 60$ kPa, $p_3 = 80$ kPa; (c) $p_1 = p_2 = 90$ kPa, $p_3 = 20$ kPa. The continuous solid lines are the simulations assuming negligible diffusional limitations and the dashed lines are the simulations with the consideration of intra-crystalline diffusion effects. For this purpose we take $\frac{D_1}{r_c^2} = \frac{D_2}{r_c^2} = 0.0005\ s^{-1}$. A video animation of the transient breakthrough at 323 K and $p_1 = p_2 = 90$ kPa, and $p_3 = 20$ kPa is available as Supplementary material.

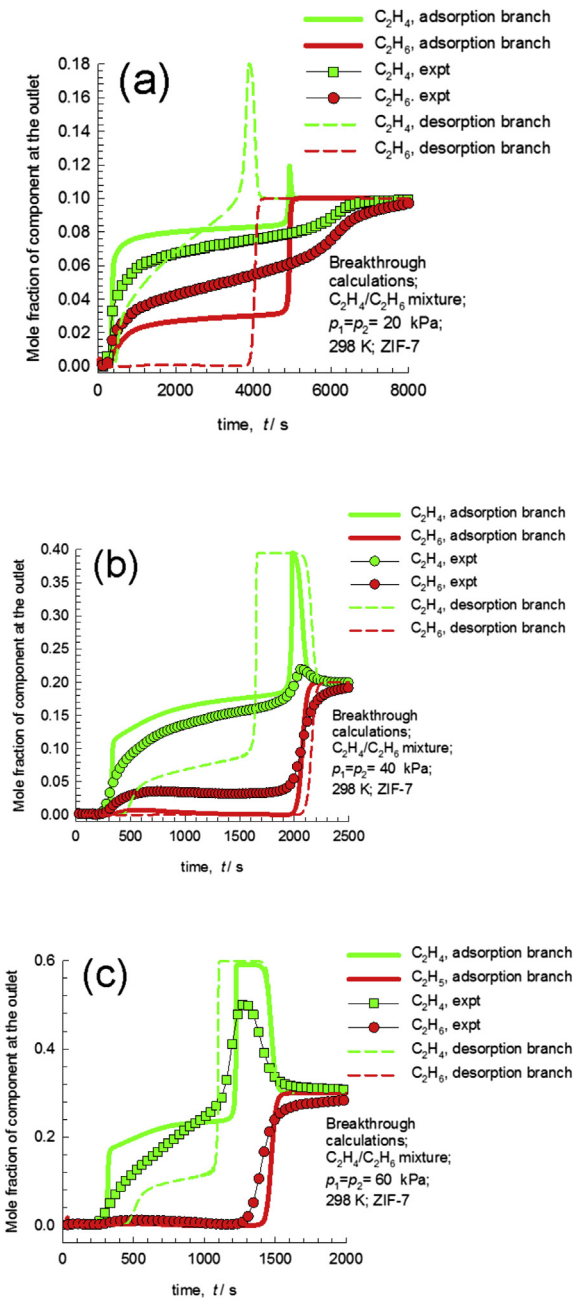

Fig. 11. Comparison of the experimental breakthroughs (the same as those in Fig. 9) with two scenarios for the simulations at 298 K: Scenario A using the "adsorption" branch of the isotherm fits (these are indicated by the continuous solid lines) and Scenario B using the "desorption" branch of the isotherm fits (these are indicated by the dashed lines).

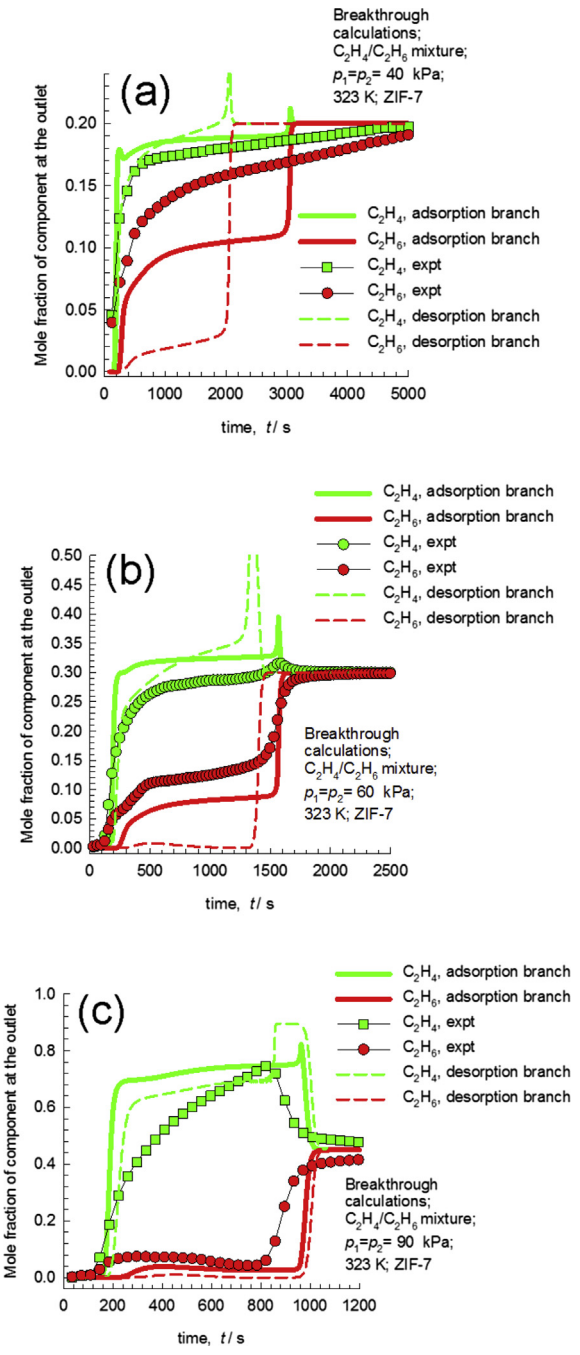

Fig. 12. Comparison of the experimental breakthroughs (the same as those in Fig. 10) with two scenarios for the simulations at 323 K: Scenario A using the "adsorption" branch of the isotherm fits (these are indicated by the continuous solid lines) and Scenario B using the "desorption" branch of the isotherm fits (these are indicated by the dashed lines).

using the "adsorption" branch of the isotherm fits (these are indicated by the continuous solid lines) and Scenario B using the "desorption" branch of the isotherm fits (these are indicated by the dashed lines). For both Scenarios A and B, we ignore diffusional limitations and invoke Eq. (S9). The differences in the breakthrough characteristics using the "adsorption" and "desorption" branches of the isotherm fits can be ascribed to the influence of the gate opening.

Fig. 11a–c represents the simulation results for breakthrough Runs 1, 2, and 3 with increasing the partial pressures of the hydrocarbons in the inlet gas stream at 298 K. On visual inspection, we conclude that the predictions of Scenario A are somewhat better than the corresponding predictions of Scenario B. The general trend observed is that the differences in the breakthrough characteristics obtained with Scenarios A and B are significantly stronger for operations with lower hydrocarbon partial pressures in the inlet stream; this is to be expected. For Run 3, for example, the breakthrough of C_2H_6 is practically indistinguishable for Scenarios A and B. It is also interesting to note for Run 3 that the experimental breakthroughs for C_2H_4 lie in between the predictions of Scenarios

A and B. This indicates that there is a progressive influence of the gate opening on the breakthrough characteristics of C_2H_4.

Fig. 12a–c represents the simulation results for breakthrough Runs 1, 2, and 3 with increasing the partial pressures of the hydrocarbons in the inlet gas stream at 323 K. A visual inspection clearly leads to the conclusion that the predictions of Scenario A are significantly better than the corresponding predictions of Scenario B for Runs 1, 2, and 3. This would indicate that the gates are entirely "open" for all the three experiments at 323 K.

The major conclusions that we draw are that the separations of C_2H_4/C_2H_6 mixtures in ZIF-7 can be predicted reasonably well using adsorption equilibrium thermodynamics. It is also clear from the analysis in Figs. 11 and 12 that for the breakthroughs at 323 K are the best understood on the basis that the gates of ZIF-7 are completely "open". For operations at 298 K, the gate-opening effect is much stronger at lower hydrocarbon pressures, as used in Run 1.

4. Conclusions

A comprehensive experimental and theoretical method has been employed to investigate the selective separation of C_2H_6 from C_2H_6/C_2H_4 mixtures utilizing the gate-opening effect of ZIF-7. The adsorption-desorption isotherms of C_2H_6 and C_2H_4 in ZIF-7 are well described by the DSLF model. The analysis of the experimental breakthroughs shows that an increase in temperature from 298 to 323 K slightly reduces the adsorption selectivity while the adsorption selectivity is increased with increasing pressure. The selectivities predicted by IAST are in reasonable agreement with the ones experimentally determined from the measured breakthroughs. The increase in adsorption selectivity with pressure could be ascribed to the fact that the adsorbed C_2H_4 molecules are replaced with adsorbing C_2H_6 molecules due to the higher adsorption affinity to C_2H_6 in ZIF-7. In addition, a comparison of the experimental breakthroughs with the breakthrough simulations shows that the consideration of the intra-crystalline diffusion does not have a significant impact on the breakthrough simulations, indicating that the separations of C_2H_6/C_2H_4 mixtures in ZIF-7 can be reasonably predicted using adsorption equilibrium thermodynamics. The current results indicate that ZIF-7 is a potential candidate for the selective separation of C_2H_6/C_2H_4 mixtures, where the concentrated C_2H_4 can be recovered in the adsorption cycle.

Acknowledgements

W. Z. and D. C. gratefully acknowledge the support from the National Natural Science Foundation of China (21036006, 21303165, and 21476214).

Appendix A. Supplementary data

Supplementary data related to this article can be found at http://dx.doi.org/10.1016/j.micromeso.2015.01.019.

Nomenclature

A	cross-sectional area of the breakthrough column, m^2
b_A	equilibrium constant in the DSLF isotherm on site A, $Pa^{-\nu_A}$
b_B	equilibrium constant in the DSLF isotherm on site B, $Pa^{-\nu_B}$
c_i	molar concentration of species i in gas mixture, mol m^{-3}
c_{i0}	molar concentration of species i in gas mixture at inlet to adsorber, mol m^{-3}
c_t	total molar concentration of gas mixture, mol m^{-3}
d	inside diameter of the packed bed column, m
$Đ_i$	Maxwell–Stefan diffusivity of species i, m^2 s^{-1}
L	length of packed bed adsorber, m
m_{ads}	mass of adsorbent packed into the breakthrough apparatus, kg
n	number of species in the mixture, dimensionless
p	pressure, Pa
p_i	partial pressure of species i in mixture, Pa
p_t	total system pressure, Pa
Q_{He}	volumetric flow rate of the inert gas He, m^3 s^{-1}
q	adsorbed amount, mol kg^{-1}
q^{abs}	absolute loading, mol kg^{-1}
q^{excess}	excess loading, mol kg^{-1}
$q_{A,sat}$	saturation capacity in the DSLF isotherm on site A, mol kg^{-1}
$q_{B,sat}$	saturation capacity in the DSLF isotherm on site B, mol kg^{-1}
q_i	component molar loading of species i, mol kg^{-1}
q_t	total molar loading in mixture, mol kg^{-1}
r_c	radius of crystallite, m
R	gas constant, 8.314 J mol^{-1} K^{-1}
Q_{st}	isosteric heat of adsorption, J mol^{-1}
S_{ads}	adsorption selectivity, dimensionless
t	time, s
T	temperature, K
t_{ss}	total period of time till the steady-state is reached, s
V	volume of the empty breakthrough column, m^3
V_{ads}	volume of adsorbent packed into the breakthrough apparatus, m^3
V_{pore}	pore volume of adsorbent, m^3 kg^{-1}
y_i	mole fraction of component i in bulk gas phase, dimensionless
z	compressibility factor in gas equation of state, dimensionless

Greek letters

ε	voidage of packed bed, dimensionless
ν_A	exponent in the DSLF isotherm on site A, dimensionless
ν_B	exponent in the DSLF isotherm on site B, dimensionless
ρ	framework density, kg m^{-3}

References

[1] R.B. Eldridge, Ind. Eng. Chem. Res. 32 (1993) 2208–2212.
[2] R. Krishna, Micropor. Mesopor. Mater. 185 (2014) 30–50.
[3] Y.B. He, R. Krishna, B.L. Chen, Energy Environ. Sci. 5 (2012) 9107–9120.
[4] E.D. Bloch, W.L. Queen, R. Krishna, J.M. Zadrozny, C.M. Brown, J.R. Long, Science 335 (2012) 1606–1610.
[5] S.J. Geier, J.A. Mason, E.D. Bloch, W.L. Queen, M.R. Hudson, C.M. Brown, J.R. Long, Chem. Sci. 4 (2013) 2054–2061.
[6] U. Böhme, B. Barth, C. Paula, A. Kuhnt, W. Schwieger, A. Mundstock, J. Caro, M. Hartmann, Langmuir 29 (2013) 8592–8600.
[7] J.W. Yoon, I.T. Jang, K.Y. Lee, Y.K. Hwang, J.S. Chang, Bull. Korean Chem. Soc. 31 (2010) 220–223.
[8] C. Gücüyener, J. van den Bergh, J. Gascon, F. Kapteijn, J. Am, Chem. Soc. 132 (2010) 17704–17706.
[9] J. van den Bergh, C. Gücüyener, E.A. Pidko, E.J.M. Hensen, J. Gascon, F. Kapteijn, Chem. Eur. J. 17 (2011) 8832–8840.
[10] Z.R. Herm, E.D. Bloch, J.R. Long, Chem. Mater. 26 (2014) 323–338.
[11] D. Peralta, G. Chaplais, A. Simon-Masseron, K. Barthelet, C. Chizallet, A.A. Quoineaud, G.D. Pirngruber, J. Am, Chem. Soc. 134 (2012) 8115–8126.
[12] Y.S. Bae, C.Y. Lee, K.C. Kim, O.K. Farha, P. Nickias, J.T. Hupp, S.T. Nguyen, R.Q. Snurr, Angew. Chem. Int. Ed. 51 (2012) 1857–1860.
[13] Q.M. Wang, D.M. Shen, M. Bülow, M.L. Lau, S.G. Deng, F.R. Fitch, N.O. Lemcoff, J. Semanscin, Micropor. Mesopor. Mater. 55 (2002) 217–230.
[14] S. Wang, Q. Yang, C. Zhong, Sep. Purif. Technol 60 (2008) 30–35.
[15] Z.B. Bao, S. Alnemrat, L. Yu, I. Vasiliev, Q.L. Ren, X.Y. Lu, S.G. Deng, Langmuir 27 (2011) 13554–13562.
[16] W. Zhu, F. Kapteijn, J.A. Moulijn, M.C. den Exter, J.C. Jansen, Langmuir 16 (2000) 3322–3329.
[17] W. Zhu, F. Kapteijn, J.A. Moulijn, Chem. Commun. (1999) 2453–2454.
[18] M. Palomino, A. Cantín, A. Corma, S. Leiva, F. Rey, S. Valencia, Chem. Commun. (2007) 1233–1235.

[19] K.H. Li, D.H. Olson, J. Seidel, T.J. Emge, H.W. Gong, H.P. Zeng, J. Li, J. Am. Chem. Soc. 131 (2009) 10368–10369.
[20] F.A. Da Silva, A.E. Rodrigues, AIChE J. 47 (2001) 341–357.
[21] C.A. Grande, F. Poplow, A.E. Rodrigues, Sep. Sci. Technol. 45 (2010) 1252–1259.
[22] K.S. Park, Z. Ni, A.P. Côté, J.Y. Choi, R. Huang, F.J. Uribe-Romo, H.K. Chae, M. O'Keeffe, O.M. Yaghi, PNAS 103 (2006) 10186–10191.
[23] X.-C. Huang, Y.-Y. Lin, J.-P. Zhang, X.-M. Chen, Angew. Chem. Int. Ed. 45 (2006) 1557–1559.
[24] G. Lu, J.T. Hupp, J. Am. Chem. Soc. 132 (2010) 7832–7833.
[25] C. Chizallet, S. Lazare, D. Bazer-Bachi, F. Bonnier, V. Lecocq, E. Soyer, A.A. Quoineaud, N. Bats, J. Am. Chem. Soc. 132 (2010) 12365–12377.
[26] K. Zhang, R.P. Lively, C. Zhang, R.R. Chance, W.J. Koros, D.S. Sholl, S. Nair, J. Phys. Chem. Lett. 4 (2013) 3618–3622.
[27] R. Banerjee, A. Phan, B. Wang, C. Knobler, H. Furukawa, M. O'Keeffe, O.M. Yaghi, Science 319 (2008) 939–943.
[28] D. Fairen-Jimenez, S.A. Moggach, M.T. Wharmby, P.A. Wright, S. Parsons, T. Duren, J. Am. Chem. Soc. 133 (2011) 8900–8902.
[29] S.A. Moggach, T.D. Bennett, A.K. Cheetham, Angew. Chem. Int. Ed. 48 (2009) 7087–7089.
[30] L.L. Zhang, G. Wu, J.W. Jiang, J. Phys. Chem. C 118 (2014) 8788–8794.
[31] Z.Q. Hu, Y.F. Chen, J.W. Jiang, J. Chem. Phys. 134 (2011) 134705.
[32] R. Krishna, R. Baur, Sep. Purif. Technol 33 (2003) 213–254.
[33] S. Aguado, G. Bergeret, M.P. Titus, V. Moizan, C. Nieto-Draghi, N. Bats, D. Farrusseng, New. J. Chem. 35 (2011) 546–550.
[34] N. Nijem, H.H. Wu, P. Canepa, A. Marti, K.J. Balkus, T. Thonhauser, J. Li, Y.J. Chabal, J. Am. Chem. Soc. 134 (2012) 15201–15204.
[35] D.-L. Chen, N.W. Wang, F.-F. Wang, J.W. Xie, Y.J. Zhong, W.D. Zhu, J.K. Johnson, R. Krishna, J. Phys. Chem. C 118 (2014) 17831–17837.
[36] X.F. Wu, M.N. Shahrak, B. Yuan, S.G. Deng, Micropor. Mesopor. Mater. 190 (2014) 189–196.
[37] P. Zhao, G.I. Lampronti, G.O. Lloyd, E. Suard, S.A.T. Redfern, J. Mater. Chem. A 2 (2014) 620–623.
[38] W.X. Cai, T. Lee, M. Lee, W. Cho, D.Y. Han, N. Choi, A.C.K. Yip, J. Choi, J. Am. Chem. Soc. 136 (2014) 7961–7971.
[39] D.-L. Chen, H. Shang, W.D. Zhu, R. Krishna, Chem. Eng. Sci. 117 (2014) 407–415.
[40] G.D. Pirngruber, L. Hamon, S. Bourrelly, P.L. Llewellyn, E. Lenoir, V. Guillerm, C. Serre, T. Devic, ChemSusChem 5 (2012) 762–776.
[41] A. Boutin, F.X. Coudert, M.A. Springuel-Huet, A.V. Neimark, G. Ferey, A.H. Fuchs, J. Phys. Chem. C 114 (2010) 22237–22244.

A combined theoretical and experimental analysis on transient breakthroughs of C_2H_6/C_2H_4 in fixed beds packed with ZIF-7

De-Li Chen,[1] Ningwei Wang,[1] Chunhui Xu,[1] Gaomei Tu,[1] Weidong Zhu,[1*] Rajamani Krishna[2*]

[1]Key Laboratory of the Ministry of Education for Advanced Catalysis Materials, Institute of Physical Chemistry, Zhejiang Normal University, 321004 Jinhua, P. R. of China.

[2]Van‘t Hoff Institute for Molecular Sciences, University of Amsterdam, Science Park 904, 1098 XH Amsterdam, The Netherlands

Corresponding authors: Tel./fax: +86 579 82282932 (W. Zhu). E-mail addresses: weidongzhu@zjnu.cn (W. Zhu), r.krishna@contact.uva.nl (R. Krishna)

Simulation methodology for transient breakthroughs

Breakthrough simulations have recently been used to screen zeolites and MOFs for gas separations with reasonable accuracy [1-5]. The breakthrough curves for gas mixtures could be calculated by taking into account of the binary mixture adsorption isotherms estimated from IAST and a plug flow proceeds through the bed. Even though the accuracy of IAST has not been established for mixture adsorption under conditions of gate-opening, the simulated breakthrough curves of N_2O/CO_2 mixtures in ZIF-7 were reported to be in reasonable agreement with the experiments [3]. In this study, we simulate the breakthroughs of C_2H_6/C_2H_4 mixtures in ZIF-7 using the same methodology as that reported in the literature [3,4].

Fixed beds packed with pellets or crystals of nanoporous materials are commonly used for separation of mixtures (see schematic in Fig. 1 in the paper); such adsorbers are commonly operated in a transient mode, and the compositions of the gas phase and within the pellets or crystals vary with position and time. For a given separation task, transient breakthroughs provide a realistic evaluation of the efficacy of an adsorbent, as they reflect the combined influence of adsorption selectivity and capacity [1,6].

Furthermore, transient breakthroughs are influenced by both mixture adsorption equilibrium and intra-crystalline diffusion. In order to determine the extent of the relative importance of adsorption and diffusion in determining the separation performance, we perform transient breakthrough simulations and compare these with the experimental data. We describe below the simulation methodology used to perform transient breakthrough calculations.

Assuming plug flow of an *n*-component gas mixture through a fixed bed maintained under isothermal conditions, the partial pressures in the gas phase at any position and instant of time are obtained by solving the following set of partial differential equations for each of the species *i* in the gas mixture [7].

$$\frac{1}{RT}\frac{\partial p_i(t,z)}{\partial t} = -\frac{1}{RT}\frac{\partial\left(v(t,z)p_i(t,z)\right)}{\partial z} - \frac{(1-\varepsilon)}{\varepsilon}\rho\frac{\partial \bar{q}_i(t,z)}{\partial t}; \quad i = 1,2,...n \tag{S1}$$

In Eq. (S1), t is the time, z is the distance along the adsorber, ρ is the framework density, ε is the bed voidage, v is the interstitial gas velocity, and $\bar{q}_i(t,z)$ is the *spatially averaged* molar loading within the ZIF-7 pellet with radius r_c, monitored at position z, and at time t.

At any time t, during the transient approach to thermodynamic equilibrium, the spatially averaged molar loading within the pellet with radius r_c is obtained by integration of the radial loading profile

$$\bar{q}_i(t) = \frac{3}{r_c^3}\int_0^{r_c} q_i(r,t)r^2 dr \tag{S2}$$

For transient unary uptake within a pellet at any position and time with the fixed bed, the radial distribution of molar loadings, q_i, within a spherical pellet with radius r_c, is obtained from a solution of a set of differential equations describing the uptake

$$\frac{\partial q_i(r,t)}{\partial t} = -\frac{1}{\rho}\frac{1}{r^2}\frac{\partial}{\partial r}\left(r^2 N_i\right) \tag{S3}$$

The molar flux N_i of component i is described by the simplified version of the Maxwell-Stefan equations in which both correlation effects and thermodynamic coupling effects are considered to be of negligible importance [1]

$$N_i = -\rho Đ_i \frac{\partial q_i}{\partial r} \tag{S4}$$

Summing Eq. (S1) over all n species in the mixture allows calculation of the *total average* molar loading of the mixture within the pellet

$$\bar{q}_t(t,z) = \sum_{i=1}^{n}\bar{q}_i(t,z) \tag{S5}$$

The *interstitial* gas velocity is related to the *superficial* gas velocity by

$$v = \frac{u}{\varepsilon} \tag{S6}$$

In industrial practice, the most common operation is to use a step-wise input of mixtures to be separated into an adsorber bed that is initially free of adsorbates, *i.e.* we have the initial conditions

$$t = 0; \quad q_i(0, z) = 0 \tag{S7}$$

At time, $t = 0$, the inlet to the adsorber, $z = 0$, is subjected to a step input of the n-component gas mixture and this step input is maintained till the end of the adsorption cycle when steady-state conditions are reached.

$$t \geq 0; \quad p_i(0, t) = p_{i0}; \quad u(0, t) = u_0 \tag{S8}$$

where u_0 is the superficial gas velocity at the inlet to the adsorber.

More details of the numerical procedures used in this work are provided by Krishna and co-workers [7-9].

If the value of $\frac{Đ_i}{r_c^2}$ is large enough to ensure that intra-crystalline gradients are absent and the entire pellet can be considered to be in thermodynamic equilibrium with the surrounding bulk gas phase at that time t and position z of the adsorber

$$\bar{q}_i(t, z) = q_i(t, z) \tag{S9}$$

The molar loadings at the *outer surface* of the pellet, *i.e.* at $r = r_c$, are calculated on the basis of adsorption equilibrium with the bulk gas phase partial pressures p_i at that position z and time t. The adsorption equilibrium can be calculated on the basis of IAST.

When matching the experimental data on breakthroughs, the parameter values used correspond to those relevant to the experiments being simulated. Two types of breakthrough simulations were performed for each experimental run: (a) including diffusional limitations with assumed values of

$\frac{Đ_i}{r_c^2}$ for matching with experimental breakthroughs and (b) assuming negligible diffusional limitations and invoking Eq. (S9).

Nomenclature

$Đ_i$ Maxwell-Stefan diffusivity of species *i*, $m^2\ s^{-1}$

L length of the packed bed adsorber, m

d inside diameter of the packed bed column, m

m_{ads} mass of adsorbent packed into the breakthrough apparatus, kg

n number of species in the mixture, dimensionless

N_i molar flux of species *i*, $mol\ m^{-2}\ s^{-1}$

p_i partial pressure of species *i* in mixture, Pa

q_i component molar loading of species *i*, $mol\ kg^{-1}$

q_t total molar loading in mixture, $mol\ kg^{-1}$

$\bar{q}_i(t)$ *spatially averaged* component molar loading of species *i*, $mol\ kg^{-1}$

r_c radius of crystallite, m

R gas constant, 8.314 $J\ mol^{-1}\ K^{-1}$

t time, s

T temperature, K

u superficial gas velocity in the packed bed, $m\ s^{-1}$

v interstitial gas velocity in the packed bed, m s^{-1}

z space coordinate, m

Greek letters

ε voidage of packed bed, dimensionless

ρ framework density, kg m^{-3}

References:

[1] R. Krishna, Micropor. Mesopor. Mater. 185 (2014) 30-50.

[2] E.D. Bloch, W.L. Queen, R. Krishna, J.M. Zadrozny, C.M. Brown, J.R. Long, Science 335 (2012) 1606-1610.

[3] D.-L. Chen, N.W. Wang, F.-F. Wang, J.W. Xie, Y.J. Zhong, W.D. Zhu, J.K. Johnson, R. Krishna, J. Phys. Chem. C 118 (2014) 17831-17837.

[4] D.-L. Chen, H. Shang, W.D. Zhu, R. Krishna, Chem. Eng. Sci. 117 (2014) 407-415.

[5] R. Krishna, J.R. Long, *J. Phys. Chem. C* 115 (2011), 12941-12950.

[6] J.W. Yoon, I.T. Jang, K.Y. Lee, Y.K. Hwang, J.S. Chang, Bull. Korean Chem. Soc. 31 (2010) 220-223.

[7] R. Krishna, R. Baur, Sep. Purif. Technol. 33 (2003) 213-254.

[8] Y.B. He, R. Krishna, B.L. Chen, Energy Environ. Sci. 5 (2012) 9107-9120.

[9] R. Krishna, R. Baur, Diffusion, Adsorption and Reaction in Zeolites: Modelling and Numerical Issues, http://krishna.amsterchem.com/zeolite/, University of Amsterdam, Amsterdam, 1 January 2015.